JOURNAL OF GEOPHYSICAL RESEARCH, VOL. 115, A00E25, doi:10.1029/2009JA014688, 2010

Click Here for Full Article

Vibrational kinetics of air plasmas induced by sprites

F. J. Gordillo-Vazquez[1]

Received 28 July 2009; revised 18 November 2009; accepted 4 January 2010; published 12 May 2010.

[1] The vibrational kinetics of air plasmas produced by the presence of sprites in the mesosphere of the Earth is studied in detail. The present model solves the coupled electron Boltzmann equation and rate equations for electrons, neutrals (ground and excited), and ions. Special attention is paid to the vibrational kinetics of N_2 ($X^1\Sigma_g^+$) and to that of the N_2 triplet states ($A^3\Sigma_u^+$, $B^3\Pi_g$, $C^3\Pi_u$, $W^3\Delta_u$, and $B'^3\Sigma_u^+$). The results presented are for an altitude of 78 km over sea level where the model-predicted vibrational distribution function (VDF) of N_2 ($B^3\Pi_g$) is in agreement with available VDF derived from sprite spectra (640–820 nm) obtained using spectrographs coupled to high-speed video cameras (300 frames per second (fps)). In addition, the model predictions indicate that the sprite plasma VDFs of N_2 ($B^3\Pi_g$) and N_2 ($C^3\Pi_u$) are almost in thermal equilibrium and exhibit a maximum at v = 0 followed by lower values for v = 1 and v = 2. Finally, it is also predicted that the N_2 ($B^3\Pi_g$) and N_2 ($C^3\Pi_u$) VDFs recorded with very high speed video cameras (up to 10000 fps) should not differ much from the N_2 ($B^3\Pi_g$) and N_2 ($C^3\Pi_u$) VDFs obtained with cameras working at lower speeds (30 and 300 fps).

Citation: Gordillo-Vazquez, F. J. (2010), Vibrational kinetics of air plasmas induced by sprites, *J. Geophys. Res.*, *115*, A00E25, doi:10.1029/2009JA014688.

1. Introduction

[2] The first spectral measurements of sprites were carried out simultaneously during the summer of 1995 by *Hampton et al.* [1996] and *Mende et al.* [1995]. The latter two groups independently reported red emission from the N_2 first positive system ($1PN_2$), that is, transitions between the excited N_2 ($B^3\Pi_g$) state and the metastable N_2 ($A^3\Sigma_u^+$) detected in a spectral range between 450 nm and 800 nm (840 nm in the case of *Hampton et al.* [1996]), and with original spectral resolutions of 2 nm [*Hampton et al.*, 1996], 6 nm [*Hampton et al.*, 1996] and 9 nm [*Mende et al.*, 1995]. The temporal resolution used by both groups was of 33 ms given by standard video recording at 30 frames per second. The work by *Green et al.* [1996] focused on the analysis of the results previously reported by *Hampton et al.* [1996] and *Mende et al.* [1995]. The results by *Green et al.* [1996] were the first to discuss the possible nature of the different molecular excitation mechanisms present in sprites and to provide some quantitative analysis on the relative populations of N_2 ($B^3\Pi_g$) vibrational levels up to v = 10 derived from the data reported by *Mende et al.* [1995] and *Hampton et al.* [1996]. However, the results concerning the emission from N_2 first positive system presented by *Mende et al.* [1995] and *Hampton et al.* [1996] mostly covered $\Delta v = 2$, 3 and 4, and only a few transitions from the $\Delta v = 1$ bands that allowed little experimental information on the v = 0 and v = 1 relative populations. The results published by *Morrill et al.* [1998] extended the spectral range to the very near infrared (900 nm) allowing the first observational insight on the relative population of v = 1 of N_2 ($B^3\Pi_g$) in sprites though at a very low altitude (53–57 km). *Morrill et al.* [1998] (and later on *Bucsela et al.* [2003]) experimentally showed that the vibrational populations of the N_2 ($B^3\Pi_g$) associated to sprite spectra at 57 km peaks at v = 2 (although this result might be probably due to sensitivity calibration errors as mentioned by *Bucsela et al.* [2003]); however, the same vibrational populations of N_2 ($B^3\Pi_g$) recorded at 53 km by *Bucsela et al.* [2003] did not exhibit any enhancement at v = 2. Recent results by *Kanmae et al.* [2007] with an improved temporal resolution of 3 ms (working with a spectral resolution of 3 nm) showed some differences between the VDF of N_2 ($B^3\Pi_g$) (up to v = 7) observed at different altitudes (between 52.7 km and 84 km). However, an opposite dependence with altitude was earlier reported by *Bucsela et al.* [2003]. Thus, the altitude effect on the VDF of N_2 ($B^3\Pi_g$) is not yet well understood.

[3] It is also worth mentioning that *Green et al.* [1996] modeled the expected radiance levels and vibrational distributions (of N_2 ($B^3\Pi_g$) and N_2^+($A^2\Pi_u$)) at 70 km as a function of electron energy. The latter allowed *Green et al.* [1996] to publish the first estimate of electron energies in sprites in a range between 0.4 eV to 2 eV. The N_2 ($B^3\Pi_g$) state vibrational distribution was best matched using a 1 eV Boltzmann electron distribution function. The 1 eV energy estimate by *Green et al.* [1996] led *Heavner et al.* [2000] to an overestimate of the total energy in a sprite of 1.2 GJ. This was largely because of the significant enhancement in vibrational excitation over electronic excitation at the lower (1 eV) energy than in the case at higher energies (2 eV and above).

[4] We present in this paper the results of a kinetic model analyzing the vibrational kinetics of sprite induced air plasmas in the Earth mesosphere. We have deduced vibrational

[1]Instituto de Astrofísica de Andalucía, CSIC, Granada, Spain.

Copyright 2010 by the American Geophysical Union.
0148-0227/10/2009JA014688

distribution functions at 78 km for the ground electronic state and some triplet electronic states of N_2 (including $A^3\Sigma_u^+$ and $C^3\Pi_u$) and, in particular, of N_2 ($B^3\Pi_g$) up to v = 6 (starting in v = 0). The results of the model exhibits a very good agreement with available VDF of N_2 ($B^3\Pi_g$) for the observed vibrational levels (from v = 2 to v = 6) and predicts no enhancement of v = 2 contrary to controversial observations at 57 km (due to possible errors in the instrument sensitivity calibration above 850 nm) [*Bucsela et al.*, 2003] but in agreement with more certain results at 53 km [*Bucsela et al.*, 2003]. In addition, the model provides the detailed kinetic mechanisms underlying the behavior of N_2 ($B^3\Pi_g$, v = 2) together with further predictions about the shape of the VDFs of N_2 ($B^3\Pi_g$) and N_2 ($C^3\Pi_u$) as they should eventually appear when sprite spectra were recorded by high-speed video cameras at 1000 frames per second (fps) and 10000 fps in future observational campaigns.

2. Kinetic Model

[5] The approach used to model the kinetics of air plasmas induced by sprites in the Earth mesosphere is firmly based on the present understanding of the chemical activity of sprites and how this activity influences the surrounding atmosphere [*Gordillo-Vazquez*, 2008; *Sentman et al.*, 2008; *Kamaratos*, 2009]. This model assumes that most of the chemical activity due to sprites begins in their brightest regions, that is, in their initial and very short living streamer heads. The duration of the sprite streamer heads have not yet been completely resolved in time but recent sprite imaging at 10000 frames per second (with 50 μs exposure time) [*McHarg et al.*, 2007; *Stenbaek-Nielsen et al.*, 2007; *Stenbaek-Nielsen and McHarg*, 2008] shows the expected point-like structure of the streamer heads. Thus, faster recordings at 20000 or perhaps even 50000 frames per second would be needed to completely resolve the time scale of sprite streamer heads. Therefore, the present kinetic model of sprite discharges considers sprites as impulsive discharges in air with pulse duration of 5 μs.

[6] In connection with the energetics of sprites, the first electron energy estimates (comparing model results and sprite spectra) were published by *Green et al.* [1996] with electron energy values between 0.4 eV to 2 eV for altitudes of 70 km. Later on, the work by *Morrill et al.* [2002] showed that the characteristic electron energies at altitudes below 55 km was ~2.2 eV, while they reached a minimum of ~1.75 eV at 60 km. More recent measurements (100 μs average) by the ISUAL instrument on board the FORMOSAT-2 satellite [*Kuo et al.*, 2005] have shown that the average electron energies in the luminous regions of sprites are between 6.2 eV and 9.2 eV. This finding suggests that, in a first stage, electrons are capable of generating a considerable degree of excitation and ionization in the low-temperature air plasmas confined within the streamer tips and, consequently, an important number of atmospheric species can become chemically active through (initially) electron-driven reactions. Later on, after the initial pulse (or sequence of pulses) has taken place, chemical activity propagates through different types of heavy-heavy reactions involving ions, as well as ground, electronically and vibrationally excited species.

[7] The reduced electric field E/N underlying the brightest sprite optical emissions has been recently estimated with the six-color spectrophotometer (SP) of the ISUAL instrument by studying $2PN_2/1NN_2^+$ ratios of several sprites observed between an altitude of 40 and 60 km and the reported E/N fields range between 243 Td and 443 Td (2.1–3.7 E_k/N, where E_k/N = 128 Td is the atmosphere breakdown reduced electric field and N is the gas density) [*Kuo et al.*, 2005]. The upper limit of the E/N values reported [*Kuo et al.*, 2005] is in agreement with the electric field magnitudes (>3 E_k/N) predicted in recent models of sprite streamers [*Liu et al.*, 2006]. However, a more recent work [*Adachi et al.*, 2008] using the blue to red (*B*/*R*) emission ratios observed by the dual-color array photometer (AP) of the ISUAL instrument indicates that the peak values of the reduced electric fields are 59–149 Td in the upper-diffuse region of sprites (above around 75 km) and 98–380 Td in the sprite lower-streamer-like region (below around 75 km). The discrepancy between the peak E/N value reported by using the spectrophotometer or the array photometer of ISUAL is claimed to be due to the different wavelengths observed [*Adachi et al.*, 2008].

2.1. Model Equations

[8] The model equations describing the non-equilibrium air plasma chemistry induced by sprites during the initial stage (streamer heads) and in the afterglow have already been introduced and described in detail in a previous work [*Gordillo-Vazquez*, 2008]. The numerical integrator chosen is an important point since its robustness is crucial for keeping the stiff stability [*Gear*, 1971] that generally appears when solving highly nonlinear set of equations as those describing the kinetics of sprite induced air plasmas once the concentrations of the fast chemical components in the discharge have decayed to negligible values. In this case, the Livermore solver for ordinary differential equations (LSODE) has been used. It can be freely downloaded from LLNL at https://computation.llnl.gov/casc/software.html.

2.2. Model Assumptions, Parameters, and Initial Conditions

[9] The present kinetic model solves the coupled Boltzmann transport equation (to derive the electron energy distribution function (EEDF)) with the rate equations associated to each of the different species considered (electrons, ions, atoms and molecules) and each of the electronically and vibrationally excited species. In this way, all the kinetics are self-consistent, although, in the present approach, the electrodynamics is not consistently solved with the plasma kinetics since the Poisson equation is not considered. In this regard, it has been assumed that the reduced electric field (E/N) within the streamer head plasma is an external parameter of the model and that it exhibits a step-like shape, that is, E/N = 400 Td (~3.3 E_k/N) during a short time interval of t_p = 5 μs while, afterward, E/N = 30 Td. The low field value after the pulse is characteristic of the afterglow region recently observed behind sprite streamer heads [*McHarg et al.*, 2007] so that the electron-driven kinetics becomes of a secondary importance when compared to the processes controlled by the collisions between ground and excited heavy species. Another important assumption of the kinetic model is related to the exclusion of photochemistry processes occurring in sprites. Some photochemical mechanisms, like photoionization, might impact the propagation and branching of sprite streamers [*Liu and Pasko*, 2004; *Bourdon et al.*, 2007] but

with an indirect or minor influence on the non-equilibrium chemistry of the streamer plasma.

[10] The transport of electrons and ions by diffusion has not been considered because their time scales are usually longer than those of the kinetic reactions controlling the concentrations of electrons and most of the ions and neutrals and, consequently, the densities of most of the species have decayed to negligible values before their transport by diffusion starts to be noticeable [*Gordillo-Vazquez*, 2008].

[11] The present calculations have been carried for an altitude of 78 km ($T_g = 200$ K). In addition, all the calculations are conducted for midnight conditions in midlatitude regions (+38 ° N), and 0° longitude, using as initial values for the neutral species listed in Appendix A those provided by the latest version (v3) of the Whole Atmosphere Community Climate Model (WACCM) based on the National Center for Atmospheric Research's Community Atmospheric Model (CAM) [*Collins et al.*, 2004]. Details on CAM are available at http://www.ccsm.ucar.edu/models/.

2.3. Kinetic Scheme and Chemical Species

[12] All the chemical species considered in the present work are listed in Appendix A, including the vibrationally excited N_2 corresponding to its ground singlet state and the five lowest electronic (triplet) states. A total of 84 ionic, atomic and molecular species with more than 700 reactions have been taken into account. The list of all the reactions considered is divided into two groups: (1) reactions involving nonvibrationally excited species and (2) processes involving vibrationally excited chemical species. The complete list of reactions of type 1 can be found in Appendix B of *Gordillo-Vazquez* [2008] excluding the processes involving Ar ($^3P_2$), $N_2^+(B^2\Sigma_u^+)$, O_4^+, N_3^+, $N_2O_5^+$ and H_2O (or H-containing species) that were not considered in the present work. The reactions of type 2, that is, those involving vibrationally excited species, are associated to a number of processes, as follows:

[13] 1. Electron-impact excitation of vibrational states of N_2 ($A^3\Sigma_u^+$), N_2 ($B^3\Pi_g$), N_2 ($W^3\Delta_u$) N_2 ($B'^3\Sigma_u^-$) and N_2 ($C^3\Pi_u$) given by

$$N_2\left(X^1\Sigma_g^+, v=0\right) + e \rightarrow N_2\left(A^3\Sigma_u^+, v=0-16\right) + e \quad (1)$$

$$N_2\left(X^1\Sigma_g^+, v=0\right) + e \rightarrow N_2\left(B^3\Pi_g, v=0-6\right) + e \quad (2)$$

$$N_2\left(X^1\Sigma_g^+, v=0\right) + e \rightarrow N_2\left(W^3\Delta_u, v=0-3\right) + e \quad (3)$$

$$N_2\left(X^1\Sigma_g^+, v=0\right) + e \rightarrow N_2\left(B'^3\Sigma_u^-, v=0-1\right) + e \quad (4)$$

and

$$N_2\left(X^1\Sigma_g^+, v=0\right) + e \rightarrow N_2\left(C^3\Pi_u, v=0-4\right) + e \quad (5)$$

The cross sections needed to numerically calculate the rate coefficients of reactions (1)–(4) using the non-equilibrium electron energy distribution function (EEDF) obtained from the solution of the Boltzmann equation coupled to the rate equations of all the species (ground, electronically and vibrationally excited) are derived using as input data the integral electron impact cross sections of the electronic states $A^3\Sigma_u^+$, $B^3\Pi_g$, $W^3\Delta_u$ and $B'^3\Sigma_u^+$ of N_2 as published by *Cartwright et al.* [1977] and, afterward, the procedure described by *Borst and Chang* [1973] to extract absolute electron impact cross sections for the excitation of individual vibrational levels of the electronic states $A^3\Sigma_u^+$, $B^3\Pi_g$, $W^3\Delta_u$ and $B'^3\Sigma_u^+$ of N_2. On the other hand, the electron impact excitation of the N_2 ($C^3\Pi_u$, v = 0–4) state from the ground N_2 ($X^1\Sigma_g^+$, v = 0) electronic state (reaction (5)) was taken from a recent analysis by *Simek* [2002] considering recently published cross-section data for the N_2 ($C^3\Pi_u$) state.

[14] 2. The vibrational-vibrational (V-V) reactions considered in this work are given by

$$N_2\left(X^1\Sigma_g^+, v\right) + N_2\left(X^1\Sigma_g^+, w-1\right) \rightarrow N_2\left(X^1\Sigma_g^+, v-1\right) + N_2\left(X^1\Sigma_g^+, w\right) \quad (6)$$

$$N_2\left(X^1\Sigma_g^+, v\right) + CO_2 \rightarrow CO_2(001) + N_2\left(X^1\Sigma_g^+, v-1\right) \cdot (\text{with } v = 1-8) \quad (7)$$

and

$$N_2\left(X^1\Sigma_g^+, v-1\right) + CO_2(001) \rightarrow CO_2 + N_2\left(X^1\Sigma_g^+, v\right) \cdot (\text{with } v = 1-8) \quad (8)$$

where the gas temperature dependent (300 K $\leq T_g \leq$ 2000 K) rate coefficient $P^{w-1,w}_{v,\,v-1}$ for reactions (6) is given by $P^{0,\,1}{}_{1,\,0}/\alpha$ [*Guerra*, 1998], where $P^{0,\,1}{}_{1,\,0} = 6.35 \times 10^{-17} \times T_g^{3/2}$ cm^3 s^{-1} (with T_g in K) and $\alpha = 39.0625 - 1.5625 \times$ Max (v, w) if Max (v, w) < 10 and $\alpha = 25.2 + 24.1 \times ((\text{Max (v, w)} - 10)/30)^3$ if Max (v, w) $\geq$ 10. The analytic rate coefficients $P^{w-1,w}_{v,\,v-1}$ agree very well with reliable VV rate coefficients in N_2 as calculated by *Billing and Fisher* [1979] in a wide range of gas temperatures (300–2000 K). For our case, the rates considered for reactions (6) were evaluated at $T_g = 300$ K. The rates for reactions (7) and (8) with v = 1 are 3.96×10^{-13} cm^3 s^{-1} and 4.33×10^{-13} cm^3 s^{-1} [*Moore et al.* 1967], respectively, while for v > 1 the rates for processes (7) and (8) were assumed the same as the ones proposed by *Moore et al.* [1967] for v = 1.

[15] 3. The vibrational-translational (V-T) excitation processes considered are of the form

$$N_2\left(X^1\Sigma_g^+, v\right) + N_2 \rightarrow N_2\left(X^1\Sigma_g^+, v-1\right) + N_2(\text{with } v = 1-8) \quad (9)$$

$$N + NO \rightarrow N_2\left(X^1\Sigma_g^+, v=3\right) + O \quad (10)$$

$$N + NO \rightarrow N_2\left(X^1\Sigma_g^+, v=4\right) + O \quad (11)$$

$$N_2\left(X^1\Sigma_g^+, v\right) + O^+ \rightarrow NO^+ + N(\text{with } v = 0-8) \quad (12)$$

Table 1. Rate Coefficients for Vibrational Redistribution ($\Delta v = 2$) (Process (14)) and Electronic Quenching of N_2 ($A^3\Sigma_u^+$, v) by N_2 and O_2 (Process (15)) as a Function of the Vibrational Quantum Number[a]

v	Vibrational Redistribution	Quenching	
		N_2	O_2
0	0	3.70e-16	2.00e-12
1	0	3.40e-16	3.80e-12
2	5.0e-15	3.55e-16	5.00e-12
3	3.80e-14	3.55e-16	5.50e-12
4	1.28e-13	3.55e-16	6.00e-12
5	2.60e-13	3.55e-16	5.70e-12
6	5.10e-13	3.55e-16	6.50e-12
7	7.00e-13	3.55e-16	7.00e-12
8	9.00e-13	3.55e-16	5.00e-12
9	1.06e-12	3.55e-16	6.00e-12
10	1.15e-12	3.55e-16	6.20e-12
11	1.14e-12	3.55e-16	6.40e-12
12	1.14e-12	3.55e-16	6.60e-12
13	1.03e-12	3.55e-16	6.80e-12
14	8.51e-13	3.55e-16	7.00e-12
15	6.17e-13	3.55e-16	7.50e-12
16	3.70e-13	3.55e-16	7.60e-12

[a]Rate coefficients are in $cm^3\ s^{-1}$.

and

$$N_2\left(X^1\Sigma_g^+, v\right) + O \rightarrow N_2\left(X^1\Sigma_g^+, v-1\right) + O(\text{with } v = 1-8) \tag{13}$$

where the rate coefficients for reactions (9) are from *Kurnosov et al.* [2007], the rate 1.47×10^{-12} $cm^3\ s^{-1}$ for reactions (10) and (11) is given by *Gordiets and Ricard* [1993], the rates for processes (12) are from *Capitelli et al.* [2000] and, finally, the rate coefficients for deactivation of N_2 ($X^1\Sigma_g^+$, v) by oxygen atoms (O) are given by *Gordiets et al.* [1995]. It is worth mentioning here that vibrational deactivation of N_2 ($X^1\Sigma_g^+$, v) by other atmospheric molecules like O_2, N_2 and NO is also possible; however, at T_g = 200 K, which is the background gas temperature assumed at 78 km, their rates are very small when compared to the vibrational deactivation by O. If a gas heating takes place, the deactivation of N_2 ($X^1\Sigma_g^+$, v) by O_2, N_2 and NO should also be taking into account.

[16] Another possible V-T reaction would be N_2 ($X^1\Sigma_g^+$, $v < 12$) + O → N + NO; however, it is an endothermic reaction with extremely low rates when vibrational levels below 12 are considered (our case).

[17] 4. Vibrational redistribution (with $\Delta v = 2$ and $\Delta v = 3$ within the $A^3\Sigma_u^+$ state of N_2)

$$N_2\left(A^3\Sigma_u^+, v \geq 2\right) + N_2\left(X^1\Sigma_g^+, v = 0\right) \rightarrow N_2\left(A^3\Sigma_u^+, v-2\right) + N_2\left(X^1\Sigma_g^+, v = 1\right) \tag{14}$$

which rate coefficients are taken from *Morrill and Benesch* [1996]. The rates associated to vibrational redistribution within N_2 ($A^3\Sigma_u^+$) with $\Delta v = 3$ are zero up to v = 17 [*Morrill and Benesch*, 1996; J. S. Morrill, private communication, 2009]. Since v = 16 was the last vibrational level of N_2 ($A^3\Sigma_u^+$) considered in the present model, there is no need to include vibrational redistribution within N_2 ($A^3\Sigma_u^+$) with $\Delta v = 3$.

Table 2. Rate Coefficients for Electronic Quenching of N_2 ($B^3\Pi_g$, v) by N_2 and O_2 (Process (15)) and Intersystem Collisional Transfer (Process (16)) as a Function of the Vibrational Quantum Number of $B^3\Pi_g$ (v), $A^3\Sigma_u^+$ (v′), $W^3\Delta_u$ (v″), and $B'^3\Sigma_u^-$ (v‴)[a]

v	Quenching		v′	ICT- $A^3\Sigma_u^+$	v″	ICT- $W^3\Delta_u$	v‴	ICT- $B'^3\Sigma_u^-$
	N_2	O_2						
0	1.65e-12	2.00e-12	7	7.83e-12	0	1.72e-11		
1	2.40e-12	3.80e-12	8	6.14e-12	1	4.17e-11		
			9	5.21e-12				
2	3.00e-12	6.00e-12	10	2.20e-11	2	2.27e-11		
3	7.50e-12	6.50e-12	11	8.57e-12				
			12	2.78e-12				
4	7.00e-12	7.00e-12	12	9.50e-13			0	8.49e-12
			13	6.00e-12				
5	7.50e-12	6.70e-12	14	8.52e-12			1	1.17e-11
			15	2.69e-12				
6	1.00e-11	8.00e-12	15	3.68e-12			2	1.83 e-11
			16	2.81e-11				

[a]Rate coefficients are in $cm^3\ s^{-1}$. ICT, intersystem collisional transfer.

[18] 5. Electronic quenching

$$N_2(\alpha, v) + M \rightarrow N_2\left(X^1\Sigma_g^+\right) + M \tag{15}$$

where α stands for the electronic states $A^3\Sigma_u^+$, $B^3\Pi_g$, $C^3\Pi_u$, $W^3\Delta_u$, $B'^3\Sigma_u^-$ of N_2 and M (the quencher) is N_2 and O_2. The rates considered (see Tables 1, 2, and 3) are for each of the different vibrational levels taken into account, that is, for v = 0 through v = 16 of $A^3\Sigma_u^+$ (J. S. Morrill, private communication, 2009), for v = 0 through v = 6 of $B^3\Pi_g$ [*Morrill and Benesch*, 1996], for v = 0 through v = 4 of $C^3\Pi_u$ [*Simek*, 2002], for v = 0 through v = 3 of $W^3\Delta_u$ [*Morrill and Benesch*, 1996] and for v = 0 and v = 1 of $B'^3\Sigma_u^-$ [*Morrill and Benesch*, 1996].

[19] 6. Intersystem collisional transfer (ICT)

$$N_2\left(B^3\Pi_g, v\right) + N_2\left(X^1\Sigma_g^+\right) \leftrightarrow N_2\left(A^3\Sigma_u^+, W^3\Delta_u, B'^3\Sigma_u^-; v\right) + N_2\left(X^1\Sigma_g^+\right) \tag{16}$$

which forward (and backward) rate coefficients (see Table 2) for all the vibrational levels considered in this work for each of the electronic states involved are taken from *Morrill and Benesch* [1996].

[20] 7. Energy pooling

$$N_2\left(A^3\Sigma_u^+, v = 0, 1\right) + N_2\left(X^1\Sigma_g^+, w \geq 5\right) \rightarrow N_2\left(B^3\Pi_g, v'\right) + N_2\left(X^1\Sigma_g^+, w-5\right) \tag{17}$$

Table 3. Rate Coefficients for Electronic Quenching of N_2 ($C^3\Pi_u$, v), N_2 ($W^3\Delta_u$, v), and N_2 ($B'^3\Sigma_u^-$, v) by N_2 (Process (15)) as a Function of the Vibrational Quantum Number[a]

v	N_2 ($C^3\Pi_u$)	N_2 ($W^3\Delta_u$)	N_2 ($B'^3\Sigma_u^-$)
0	1.09e-11	1.65e-12	2.00e-13
1	2.90e-11	2.40e-12	3.00e-13
2	4.30e-11	3.00e-12	
3	4.80e-11		
4	4.90e-11		

[a]Rate coefficients are in $cm^3\ s^{-1}$.

Table 4. Rate coefficients for State-to-State Excitation of N_2 ($B^3\Pi_g$, v = 1–6) (Process (18)) and N_2 ($C^3\Pi_u$, v = 0–4) (Process (19)) in Energy Pooling Reactions of the Types N_2 ($A^3\Sigma_u^+$, v = 0) + N_2 ($A^3\Sigma_u^+$, v = 0) (k_{00}^B, k_{00}^C) and N_2 ($A^3\Sigma_u^+$, v = 0) + N_2 ($A^3\Sigma_u^+$, v = 1) (k_{01}^B, k_{01}^C)[a]

v	k_{00}^B	k_{00}^C	k_{01}^B	k_{01}^C
0		2.60e-11		3.40e-11
1	2.40e-11	4.10e-11	6.60e-11	5.40e-11
2	3.90e-11	4.10e-11	5.60e-11	3.30e-11
3	1.90e-11	2.80e-11	5.80e-11	2.20e-11
4	1.60e-11	1.00e-11	2.70e-11	1.00e-11
5	1.50e-11		2.20e-11	
6	1.10e-11		1.70e-11	

[a]Rate coefficients are in $cm^3\ s^{-1}$.

which rate coefficient given by 3.00×10^{-11} $cm^3\ s^{-1}$ is obtained from *Piper* [1989].

[21] The state-to-state excitation of N_2 ($B^3\Pi_g$, v′ = 1–6) and N_2 ($C^3\Pi_u$, v′ = 0–4) are also possible in energy pooling reactions between N_2 ($A^3\Sigma_u^+$, v = 0, 1) and subsequent quenching in collisions with ground state molecular nitrogen such as

$$N_2\left(A^3\Sigma_u^+, v = 0\right) + N_2\left(A^3\Sigma_u^+, v = 0, 1\right) \rightarrow N_2\left(B^3\Pi_g, v'\right) + N_2\left(X^1\Sigma_g^+\right) \quad (18)$$

and

$$N_2\left(A^3\Sigma_u^+, v = 0\right) + N_2\left(A^3\Sigma_u^+, v = 0, 1\right) \rightarrow N_2\left(C^3\Pi_u, v'\right) + N_2\left(X^1\Sigma_g^+\right) \quad (19)$$

which rate coefficients (see Table 4) are given by *Piper* [1988a] and *Piper* [1988b] for processes (18) and (19), respectively.

[22] 8. Radiative de-excitation of vibrational levels of N_2 ($B^3\Pi_g$) to N_2 ($A^3\Sigma_u^+$), that is, the N_2 first positive system ($1PN_2$) ($B^3\Pi_g \rightarrow A^3\Sigma_u^+$) is decomposed into 65 individual transitions (covering the 554 nm–3.4 μm spectral range) between vibrational levels of N_2 ($B^3\Pi_g$) and N_2 ($A^3\Sigma_u^+$), instead of considering them in a lump with every vibrational quantum number as averaged state.

$$N_2\left(B^3\Pi_g, v' \leq 6\right) \rightarrow N_2\left(A^3\Sigma_u^+, v'' \leq 16\right) + h\nu \quad (20)$$

Table 5. Radiative Transitions Considered for the N_2 First Positive System ($1PN_2$) ($B^3\Pi_g$ (v′) → $A^3\Sigma_u^+$ (v″))[a]

v′\v″	0	1	2	3	4	5	6	7	8	9	10	11	12	13
0	×	×	×	×	×									
1	×	×	×	×	×	×	×							
2	×	×	×	×	×	×	×	×						
3	×	×	×	×	×	×	×	×	×	×				
4	×	×	×	×	×	×	×	×	×	×	×			
5	×	×	×	×	×	×	×	×	×	×	×	×		
6		×	×	×	×	×	×	×	×		×	×	×	×

[a]All the transitions with Einstein coefficients $\geq 10^2\ s^{-1}$ have been taken into account. The crosses indicate that the transition has been included in the model.

Table 6. Radiative Transitions Considered for the N_2 Second Positive System ($2PN_2$) ($C^3\Pi_u$ (v′) → $B^3\Pi_g$ (v″))[a]

v′\v″	0	1	2	3	4	5	6
0	×	×	×	×	×	×	×
1	×	×	×	×	×	×	×
2	×	×	×	×	×	×	×
3	×	×	×	×	×	×	×
4	×	×	×	×	×	×	×

[a]The crosses indicate that the transition has been included in the model.

The radiative transitions probabilities of 1PN2 included (see Table 5) are all those listed in *Gilmore et al.* [1992] with transition probabilities $\geq 10^2\ s^{-1}$.

[23] 9. Radiative de-excitation of vibrational levels of N_2 ($C^3\Pi_u$) to N_2 ($B^3\Pi_g$), that is, the N_2 second positive system ($2PN_2$) ($C^3\Pi_u \rightarrow B^3\Pi_g$) is decomposed into 35 individual transitions (covering the 268 nm–503 nm spectral range) between the included vibrational levels of N_2 ($C^3\Pi_u$, v = 0–4) and N_2 ($B^3\Pi_g$, v = 0–6):

$$N_2\left(C^3\Pi_u, v' \leq 4\right) \rightarrow N_2\left(B^3\Pi_g, v'' \leq 6\right) + h\nu \quad (21)$$

The radiative transitions of $2PN_2$ included (see Table 6) are taken from *Gilmore et al.* [1992].

[24] 10. Removal of N_2 ($C^3\Pi_u$, v ≥ 1) by N_2 ($X^1\Sigma_g^+$, v = 0) as given by

$$N_2\left(C^3\Pi_u, v \geq 1\right) + N_2\left(X^1\Sigma_g^+, v = 0\right) \rightarrow N_2\left(C^3\Pi_g, v - 1\right) + N_2\left(X^1\Sigma_g^+, v = 1\right) \quad (22)$$

which rate coefficients 1.00×10^{-11} $cm^3\ s^{-1}$ (the same for N_2 ($C^3\Pi_u$, v = 1–4)) are given by *Calo and Axtmann* [1971]. For clarity, all the rate coefficients that depend on the vibrational quantum number have been shown in Tables 1–4 and 7.

3. Results and Discussion

3.1. Electron Energy Distribution Function in Sprite Plasmas

[25] A key point in this kind of kinetic modeling is the calculation of the electron energy distribution function (EEDF), its values and how it changes with time, that is, the EEDF time scale and how it compares with that of the

Table 7. Rate Coefficients for VT of N_2 ($X^1\Sigma_g^+$, v) by N_2, O^+, and O (Processes (9), (12), and (13)) as a Function of the Vibrational Quantum Number[a]

V	VT-N_2	VT-O^+	VT-O
0		1.1384e-12[b]	
1	3.5e-21	1.0500e-12	7.6901e-16
2	6.5e-21	3.5560e-11	1.1606e-15
3	1.5e-20	1.9804e-10	1.5568e-15
4	2.5e-20	2.8452e-10	1.9578e-15
5	3.5e-20	5.7732e-11	2.3634e-15
6	7.0e-20	1.6220e-10	2.7738e-15
7	1.0e-19	1.1440e-10	3.1888e-15
8	1.5e-19	1.4154e-10	3.6085e-15

[a]Rate coefficients are in $cm^3\ s^{-1}$.
[b]Read 1.1384e-12 as 1.1384×10^{-12}.

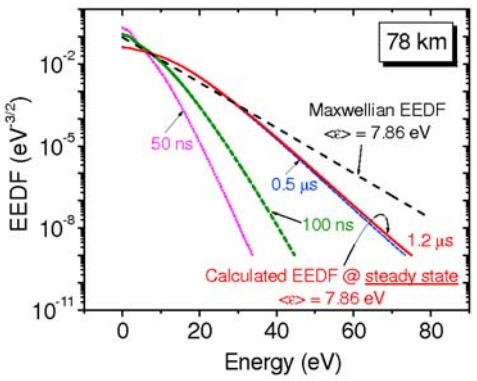

Figure 1. Time-dependent behavior of the calculated electron energy distribution function (EEDF) during the pulse at different time steps (50 ns; short dotted line; 100 ns, short dashed dotted line; 0.5 μs, dashed dotted line; 1.2 μs, solid line) and Maxwellian EEDF (dashed line).

chemical species dynamics. In addition, it is very important to determine whether the EEDF is near equilibrium; if it is close to equilibrium, the calculations are greatly simplified. These issues are crucial for kinetic modeling because, usually, the EEDF strongly conditionates the values of rate coefficients of electron-driven reactions that, in addition, influences the kinetics of heavy-heavy species. Therefore, we first present the results of a numerical solution to the transport Boltzmann equation coupled to the electron, ion, neutral (atomic and molecular) and vibrational kinetics described in sections 2.1, 2.2, and 2.3. The calculated EEDF for air plasmas produced by sprites when vibrational kinetics is considered is shown in Figure 1 for different times and for an altitude of 78 km. The impulsive discharge (representing a single sprite event) lasts 5 μs and it is clearly visible in Figure 1 that in about 1.2 μs the EEDF (with mean electron energy of 7.86 eV) reaches steady state though it is almost achieved after 0.5 μs. In addition, Figure 1 shows for comparison the shape of a Maxwellian EEDF (equilibrium case) for the same mean energy of the calculated EEDF. Figure 1 clearly shows the deviation of the calculated EEDF (solid line) from the Maxwellian one. This deviation becomes more and more important as the electron energy increases. We could conclude from Figure 1 that, in order to study the electron kinetics of sprite streamers, it is really not crucial to follow the time behavior of the EEDF since its time scale (relaxation times) is usually shorter (hundreds of nanoseconds) than that of streamer head lifetimes (microseconds). Thus, it would be enough to consider the steady state EEDF during the pulse. The latter would be justified for low field values (below, for instance, air threshold values of about 128 Td) because the relaxation times of the EEDFs are usually much faster than typical time scales in TLEs. For example, the lifetimes of streamer heads in sprites for electric fields below or near threshold values [*Mishin and Milikh*, 2008]. However, for field values well above the breakdown field, the relevant time scale is given by the width of the space charge layer in the streamer head divided by the streamer velocity which could reach values similar to the EEDF relaxation time (~0.5 μs). This is the situation for the 400 Td sprite pulse considered here. Thus, when modeling the kinetics induced by sprite streamers it is necessary to keep the temporal dependence of the EEDF rather than using its steady state values.

3.2. Electron, Ions, NO_x, and N_2O

[26] The concentrations as a function of time of electrons and some important negative ions are shown in Figure 2a, while densities of positive ions are displayed in Figure 2b. The ground state concentrations of nitrogen and oxygen atoms together with those of nitride oxides (NO_x and N_2O) are represented in Figure 2c.

[27] The concentration profiles and kinetic mechanisms for the production and loss of electrons, O^- and O_2^- at 78 km are similar to those already shown earlier for the same altitude [*Gordillo-Vazquez*, 2008]. The impact of a single sprite event occurring at 78 km on the background mesospheric electron density is to enhance it by a maximum of about one order of

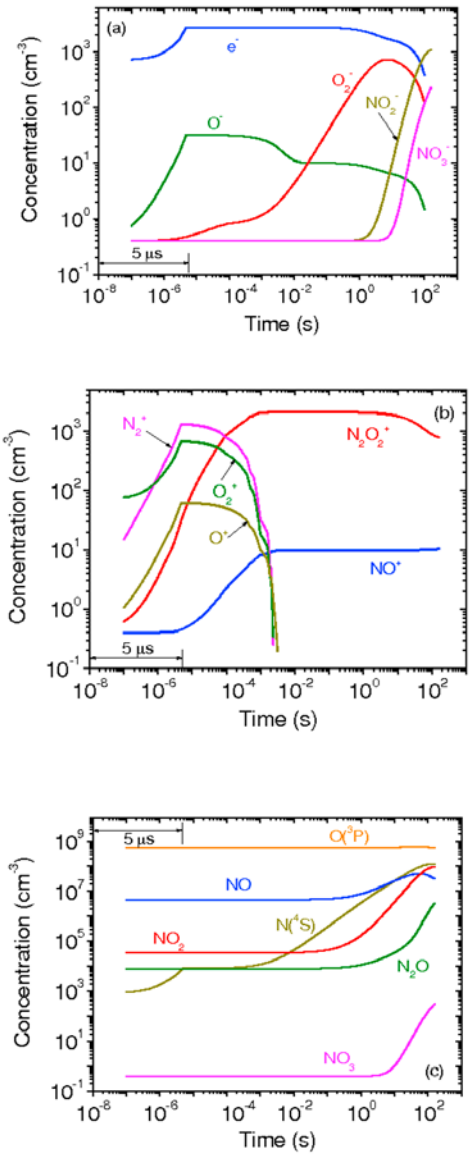

Figure 2. Calculated time-dependent behavior at 78 km of the concentrations of (a) electrons and most important negative ions considered, (b) positive ions, and (c) ground oxygen and nitrogen atoms, NO_x and N_2O.

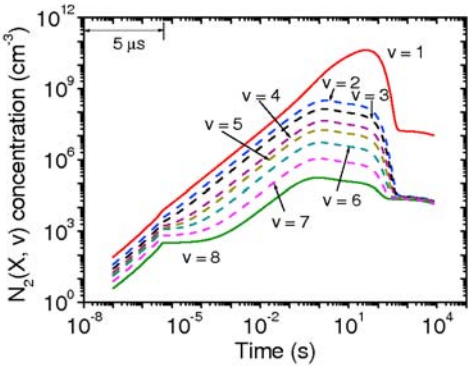

Figure 3. Calculated time-dependent concentration of the vibrational levels of $N_2(X^1\Sigma_g^+)$. The solid lines are for v = 1 and v = 8. The dashed lines are for v = 2 through v = 7. The value corresponding to v = 0 remains constant and equal to 3.1×10^{14} cm^{-3} for the time interval investigated.

magnitude up to ~3×10^3 cm^{-3}. The latter value is close to the predicted electron number density just behind the streamer head [*Liu and Pasko*, 2004]. After the impulsive phase (time > 5 μs), the density of electrons remains high mainly due to the two-body dissociative electron attachment to O_2 (O_2 + e → O^- + O) and the three-body electron attachment to O_2 (O_2 + O_2 + e → O_2^- + O_2). It is also visible in Figure 2a that the concentrations of nitride oxide negative ions such as NO_2^- and NO_3^- remain flat up to approximately one second when they exhibit a fast growth due to electron attachment to NO_2 (e + NO_2 → NO_2^-) and NO_2^- + O_3 → O_2 + NO_3^-, respectively.

[28] The variation as a function of time shown by the concentrations of most (except O^+) of the positive ions represented in Figure 2b were already described [*Gordillo-Vazquez*, 2008]. The density of O^+ closely follows that of O_2^+ and its main production channel during the pulse (time < 5 μs) is dissociative ionization of O_2 (e + O_2 → O^+ + O + 2 e) while its removal is mainly due to charge transfer reactions like $O^+ + O_2 \rightarrow O_2^+ + O$ closely followed by $N_2 + O^+ \rightarrow NO^+ +$ N. For times greater than 5 μs, the production of O^+ is dominated by the charge transfer reaction $N_2^+ + O \rightarrow N_2 + O^+$ while the loss of O^+ is controlled by $O^+ + O_2 \rightarrow O_2^+ + O$.

[29] The behavior of the concentrations of nitride oxides (including N_2O) due the impact of sprite chemical activity at a height of 78 km is shown in Figure 2c. There it can be seen that the background value of NO hardly changes while the background concentrations of NO_2, NO_3 and N_2O increases by, roughly, two orders of magnitude. According to present calculations, the main channel producing NO at 78 km is the radiative de-excitation (γ bands) of NO ($A^2\Sigma^+$) toward the ground electronic state of NO. The second most important production mechanism of NO is the charge transfer reaction $NO^- + O_2 \rightarrow O_2^- + NO$. The rest of kinetic mechanisms underlying the densities of O (^{3}P), N (^{4}S), NO, NO_2 and NO_3 shown in Figure 2c are the same as those described earlier [*Gordillo-Vazquez*, 2008]. Regarding the production of N_2O, it should be said that, for times less than 5 μs, it is driven by $O^- + N_2 \rightarrow N_2O$ + e while for times beyond the pulse duration, that is, greater than 5 μs, the reaction N_2 ($A^3\Sigma_u^+$) + O_2 → N_2O + O dominates the formation of N_2O. For times less than 5 μs, the loss of N_2O is mainly due to electron impact ionization of N_2O (e + N_2O → N_2O^+ + 2 e) followed by electron impact dissociation of N_2O (e + N_2O → N_2 + O + 2 e). For times greater than 5 μs the major loss is by charge transfer processes like $N_2^+ + N_2O \rightarrow N_2O^+ + N_2$.

3.3. Vibrational Kinetics of N_2 ($X^1\Sigma_g^+$)

[30] The concentrations of the eight vibrational levels considered in the ground electronic state of N_2 ($X^1\Sigma_g^+$) are shown in Figure 3 as a function of time. All concentrations follow a positive slope as time increases since the main excitation channel is electron vibrational excitation e + N_2 ($X^1\Sigma_g^+$, v = 0) ↔ e + N_2 ($X^1\Sigma_g^+$, v = 1–8) that keeps a high vibrational excitation since the sprite enhanced electron concentration at 78 km remains high up to about 1 s. The concentration of N_2 ($X^1\Sigma_g^+$, v = 1) begins to decrease around 10 s because by that time the process N_2 ($X^1\Sigma_g^+$, v = 1) + CO_2 → CO_2 (001) + N_2 ($X^1\Sigma_g^+$, v = 0) starts to be important. The concentrations of the higher N_2 ($X^1\Sigma_g^+$, v > 1) also begin to decrease from about 0.1 s but mainly due to the action of the VV processes N_2 ($X^1\Sigma_g^+$, v) + N_2 ($X^1\Sigma_g^+$, v = 0) → N_2 ($X^1\Sigma_g^+$, v−1) + N_2 ($X^1\Sigma_g^+$, v = 1) that dominate over N_2 ($X^1\Sigma_g^+$, v) + CO_2 → CO_2 (001) + N_2 ($X^1\Sigma_g^+$, v−1) for v > 1.

[31] Since at the beginning of the pulse we have a cold atmosphere, without vibrational or electronic excitation, the set of rate equations is solved by considering as initial conditions that, at the beginning, N_2 ($X^1\Sigma_g^+$, v = 0) = N_2, where N_2 represents the nitrogen proportion in the gas phase mixture [*Pintassilgo et al.*, 2009]. Thus, in our case, for the gas pressure and temperature used, we have that N_2 ($X^1\Sigma_g^+$, v = 0) remains constant and equal to 3.1×10^{14} cm^{-3} for the time range investigated.

[32] The vibrational distribution function (VDF) of N_2 ($X^1\Sigma_g^+$, v) at 78 km, which is the relative population of each vibrational level of N_2 ($X^1\Sigma_g^+$) as compared to the population of N_2 ($X^1\Sigma_g^+$, v = 0) is shown in Figures 4a and 4b. The VDF of N_2 ($X^1\Sigma_g^+$, v) for different times from 0.1 μs to 10 ms are shown in Figure 4a. In general, as time increases, the vibrational population of a given level grows. The latter is a logical consequence of how the vibrational kinetics works; for very short times, the system does not have enough time for electrons to pump up the different vibrational levels of N_2 ($X^1\Sigma_g^+$). On the other hand, the VDF of N_2 ($X^1\Sigma_g^+$, v) averaged over periods of times of 30 ms, 3 ms and 1 ms has been represented in Figure 4b. These time periods have been chosen because they correspond to the time resolutions of regular (30 ms or 30 frames per second (fps)) and high-speed (3 ms or 300 fps and 1 ms or 1000 fps) video recordings used in field observations of sprites. An important result from Figures 4a and 4b is that the sprite induced VDF of N_2 ($X^1\Sigma_g^+$, v) at 78 km is far from equilibrium since there is no Boltzmann (nor Treanor [*Caledonia and Center*, 1971]) VDF that could fit the shape of the calculated VDF of N_2 ($X^1\Sigma_g^+$, v) resulting from the sprite chemical activity. To appreciate deviation of calculated N_2 ($X^1\Sigma_g^+$) VDFs from equilibrium, dash-dotted straight lines in Figure 4a indicate hypothetical Boltzmann VDFs of N_2 ($X^1\Sigma_g^+$) with vibrational temperatures of 100, 200, 300, 400 and 1000 K.

3.4. Vibrational Kinetics of N_2 ($A^3\Sigma_u^+$)

[33] In order to study the vibrational kinetics of N_2 ($A^3\Sigma_u^+$) induced by sprites, the time variation of the concentrations of some vibrational levels of N_2 ($A^3\Sigma_u^+$) are shown in Figure 5. It

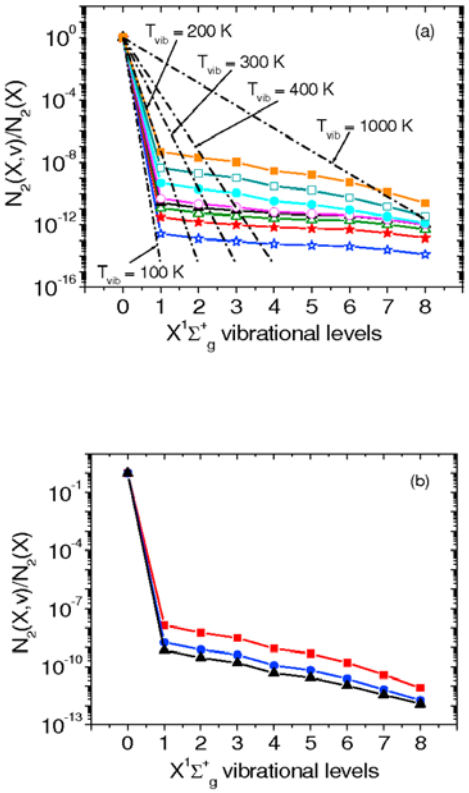

Figure 4. (a) Calculated vibrational distribution function (VDF) of N_2 ($X^1\Sigma^+_g$) for different times (10 ms, solid squares; 1 ms, open squares; 100 μs, solid circles; 10 μs, open circles; 5 μs, solid triangles; 3 μs, open triangles; 1 μs, solid stars; 0.1 μs, open stars). To appreciate deviation of calculated VDFs from equilibrium case, dash-dotted straight lines indicate hypothetical Boltzmann VDFs of N_2 ($X^1\Sigma^+_g$) with vibrational temperatures of T_{vib} = 100, 200, 300, 400, and 1000 K. (b) Calculated VDF of N_2 ($X^1\Sigma^+_g$) averaged over 30 ms (solid squares), 3 ms (solid circles), and 1 ms (solid triangles).

can clearly be seen in Figure 5 that the population of each of the considered vibrational levels of N_2 ($A^3\Sigma^+_u$) reaches its maximum value during the pulse phase (time < 5 μs) and, afterward, they remain constant up to about one millisecond to, later on, exhibit a decrease that becomes sharper for the highest vibrational levels. During the pulse (time < 5 μs), the dominant production channels of the lowest vibrational levels of the metastable N_2 ($A^3\Sigma^+_u$) state are dominated by radiative decay from N_2 ($B^3\Pi_g$, v′) to N_2 ($A^3\Sigma^+_u$, v″ = 0, 1, 2). Specific examples are, N_2 ($B^3\Pi_g$, v′ = 1) → N_2 ($A^3\Sigma^+_u$, v″ = 0) + 888.3 nm, N_2 ($B^3\Pi_g$, v′ = 3) → N_2 ($A^3\Sigma^+_u$, v″ = 1) + 760.6 nm and N_2 ($B^3\Pi_g$, v′ = 4) → N_2 ($A^3\Sigma^+_u$, v″ = 2) + 748.4 nm. The electron impact vibrational excitation from N_2 ($X^1\Sigma^+_g$, v = 0) is the prevailing production mechanism of the middle and upper vibrational levels (from v″ = 5 to v″ = 16) of N_2 ($A^3\Sigma^+_u$) [*Cartwright*, 1978].

[34] The dominant removal mechanisms during the first five microseconds are electronic quenching of N_2 ($A^3\Sigma^+_u$, v″ = 0–6) by O_2 (see processes (15)) and backward intersystem collisional transfer (ICT) of N_2 ($A^3\Sigma^+_u$, v″ = 7–16) followed by electronic quenching by O_2 to produce vibrationally excited N_2 ($B^3\Pi_g$, v′).

[35] For times beyond 5 μs, the production channels for the lowest vibrational levels of the metastable N_2 ($A^3\Sigma^+_u$) (v″ = 0–1) are dominated by radiative de-excitation from N_2 ($B^3\Pi_g$, v′). These transitions are, for 1 ms, N_2 ($B^3\Pi_g$, v′ = 0) → N_2 ($A^3\Sigma^+_u$, v″ = 0) + 1.04 μm and N_2 ($B^3\Pi_g$, v′ = 0) → N_2 ($A^3\Sigma^+_u$, v″ = 1) + 1.23 μm. The vibrational redistribution mechanism (see reactions (14)) controls the production of N_2 ($A^3\Sigma^+_u$, v′ = 2–13) and, finally, backward ICT reactions dominate the gain processes that populate N_2 ($A^3\Sigma^+_u$, v′ = 14–16). The removal scheme of N_2 ($A^3\Sigma^+_u$, v′) beyond 5 μs is the same as that described for the pulse stage (time < 5 μs).

[36] The VDF of N_2 ($A^3\Sigma^+_u$) for different times from 1 μs to 100 ms is shown in Figure 6a. In addition, Boltzmann VDFs (straight dashed lines) have been fitted to the calculated VDFs. The agreement between the Boltzmann and the calculated VDFs is reasonable so that it is possible (and reasonable) to obtain a vibrational temperature (T^A_{vib}) associated to N_2 ($A^3\Sigma^+_u$) for the different times investigated. Thus, T^A_{vib} has been represented in Figure 6b, where it can be clearly seen that the vibrational temperature associated to the $A^3\Sigma^+_u$ state of N_2 decreases from about 10000 K (~0.9 eV) at 1 μs to 3700 K (~0.35 eV) obtained for times of 100 ms. The vibrational temperature implies the degree of vibrational excitation so that, when the population of a certain level under investigation is close to its equilibrium value (given by a Boltzmann distribution), a high vibrational temperature indicates an important vibrational excitation.

[37] The calculated VDFs of N_2 ($A^3\Sigma^+_u$) averaged over periods of times of 30 ms, 3 ms and 1 ms have been represented in Figure 7 together with Boltzmann (equilibrium) VDFs indicated by straight lines. As can be seen in Figure 7, the calculated sprite induced VDFs of N_2 ($A^3\Sigma^+_u$) at 78 km are far from equilibrium. The VDFs of N_2 ($A^3\Sigma^+_u$) shown in Figure 7 are the present model predictions about how field recorded VDFs of N_2 ($A^3\Sigma^+_u$) would look like when using video cameras working at different speeds (30 fps, 300 fps and 1000 fps) coupled to imaging spectrographs tuned in the appropriate spectral range.

3.5. Vibrational Kinetics of N_2 ($B^3\Pi_g$)

[38] The understanding of the vibrational kinetics of N_2 ($B^3\Pi_g$) involved in the red emission associated to the N_2

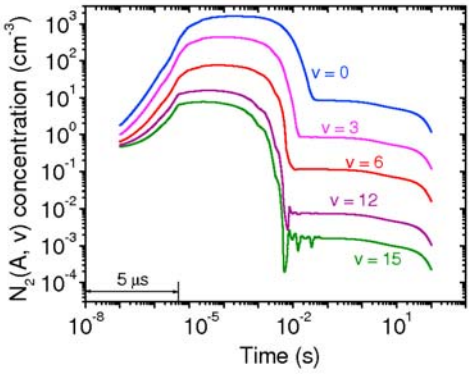

Figure 5. Calculated time-dependent concentration of the vibrational levels of N_2 ($A^3\Sigma^+_u$). Only some representative vibrational levels out of the 16 considered for $A^3\Sigma^+_u$ have been plotted.

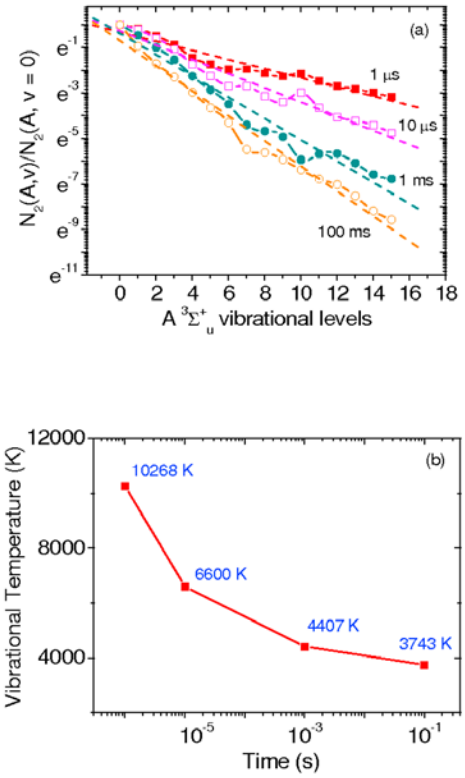

Figure 6. (a) Calculated vibrational distribution function (VDF) of N_2 ($A^3\Sigma_u^+$) for different times (1 μs, solid squares; 10 μs, open squares; 1 ms, solid circles; 10 ms and 100 ms, open circles) and corresponding fits to Boltzmann VDFs (dashed lines). (b) Calculated vibrational temperature for N_2 ($A^3\Sigma_u^+$) as a function of time derived from the Boltzmann VDF fits in Figure 6a.

first positive system ($1PN_2$) recorded during sprite observations is one of the main goals of the present paper. As mentioned in the introduction of this work, a number of articles have been published since 1995 reporting spectral observations of the characteristic red emission from sprites covering a spectral range from 450 nm up to 900 nm. *Morrill et al.* [1998] (and later on *Bucsela et al.* [2003]) experimentally showed that the vibrational populations of the N_2 ($B^3\Pi_g$) associated to sprite spectra at 57 km peaks at v = 2 (although this result might be probably due to sensitivity calibration errors as mentioned by *Bucsela et al.* [2003]). However, the same vibrational populations of N_2 ($B^3\Pi_g$) recorded by *Bucsela et al.* [2003] at 53 km under more reliable calibration conditions did not exhibit any enhancement at v = 2. To date, the kinetic mechanisms underlying the behavior under sprite conditions of the vibrational levels of N_2 ($B^3\Pi_g$) and, in particular, of N_2 ($B^3\Pi_g$, v = 2) have remained unexplained. In order to shed some light on this issue, we show in Figure 8 the results of our sprite kinetic model calculations regarding time-dependent concentrations of the different vibrational levels considered for the N_2 ($B^3\Pi_g$) state in our model. Two points are clear from Figure 8, first that all the vibrational level populations of N_2 ($B^3\Pi_g$) reach their maxima by the pulse end (5 μs) and, second, that the concentration of v = 2 is, at all times, below the concentrations of v = 0 and v = 1.

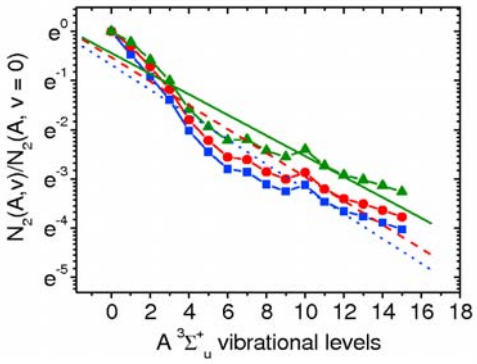

Figure 7. Calculated vibrational distribution function (VDF) of N_2 ($A^3\Sigma_u^+$) averaged over 30 ms (solid squares), 3 ms (solid circles), and 1 ms (solid triangles) and their corresponding Boltzmann VDF fits (30 ms, dotted line; 3 ms, dashed line; 1 ms, solid line).

[39] The present sprite chemical model indicates that during the pulse (time < 5 μs), the production of N_2 ($B^3\Pi_g$, v = 0–6) is mainly controlled by electron-impact excitation from ground state N_2 ($X^1\Sigma_g^+$), that is, N_2 ($X^1\Sigma_g^+$, v = 0) + e → N_2 ($B^3\Pi_g$, v = 0–6) + e, closely followed by radiative cascade de-excitation from N_2 ($C^3\Pi_u$, v = 0–4). The removal of the concentrations of N_2 ($B^3\Pi_g$, v = 0–6) is mainly due to radiative decays toward different vibrational levels of N_2 ($A^3\Sigma_u^+$) state. For times beyond 5 μs, the production of N_2 ($B^3\Pi_g$, v = 0–6) is driven by intersystem collisional transfer (ICT) processes up to about several milliseconds, then direct electron-impact excitation from N_2 ($X^1\Sigma_g^+$) becomes dominant. The mechanisms underlying the losses of N_2 ($B^3\Pi_g$, v = 0–6) beyond 5 μs are the same as the ones during the pulse.

[40] The detailed rate variations with time of the underlying production and removal channels contributing to the population density of N_2 ($B^3\Pi_g$, v = 2) have been plotted in Figures 9a and 9b, respectively. We can see in Figure 9a that process G1, that is, the electron impact excitation of N_2 ($B^3\Pi_g$, v = 2) from N_2 ($X^1\Sigma_g^+$, v = 0) dominates the production of N_2 ($B^3\Pi_g$, v = 2) during the first 5 μs (pulse duration) closely followed by radiative decay from N_2 ($C^3\Pi_u$, v = 1, 0), processes G2 and G3 and, finally, also followed by two intersystem collisional transfer reactions (with labels

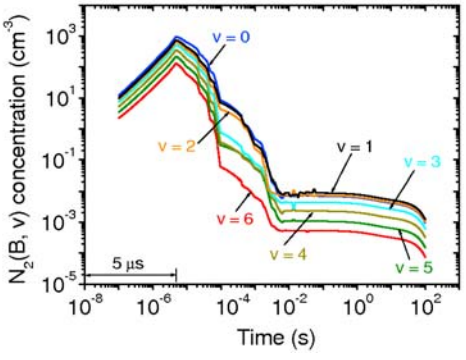

Figure 8. Calculated time-dependent concentration of the seven vibrational levels considered for N_2 ($B^3\Pi_g$).

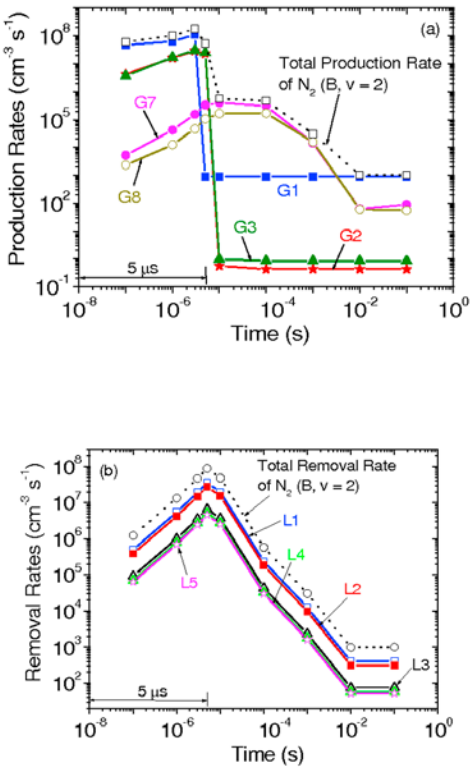

Figure 9. (a) Calculated time-dependent gain rates of N_2 ($B^3\Pi_g$) corresponding to the most important production channels: G1, N_2 ($X^1\Sigma_g^+$, v = 0) + e → N_2 ($B^3\Pi_g$, v = 2) + e; G2, N_2 ($C^3\Pi_u$, v = 1) → N_2 ($B^3\Pi_g$, v = 2) + 353.6 nm; G3, N_2 ($C^3\Pi_u$, v = 0) → N_2 ($B^3\Pi_g$, v = 2) + 380.4 nm; G7, N_2 ($W^3\Delta_u$, v = 2) + N_2 ($X^1\Sigma_g^+$) → N_2 ($B^3\Pi_g$, v = 2) + N_2 ($X^1\Sigma_g^+$); and G8, N_2 ($A^3\Sigma_u^+$, v = 10) + N_2 ($X^1\Sigma_g^+$) → N_2 ($B^3\Pi_g$, v = 2) + N_2 ($X^1\Sigma_g^+$). The dotted line represents the total production rate of N_2 ($B^3\Pi_g$). (b) Calculated time-dependent loss rates of N_2 ($B^3\Pi_g$) corresponding to the most important loss channels: L1, N_2 ($B^3\Pi_g$, v = 2) → N_2 ($A^3\Sigma_u^+$, v = 1) + 869.5 nm; L2, N_2 ($B^3\Pi_g$, v = 2) → N_2 ($A^3\Sigma_u^+$, v = 0) + 773.2 nm; L3, N_2 ($B^3\Pi_g$, v = 2) → N_2 ($A^3\Sigma_u^+$, v = 2) + 990.5 nm; L4, N_2 ($B^3\Pi_g$, v = 2) → N_2 ($A^3\Sigma_u^+$, v = 4) + 1.3275 μm; L5, N_2 ($B^3\Pi_g$, v = 2) + N_2 ($X^1\Sigma_g^+$) → N_2 ($W^3\Delta_u$, v = 2) + N_2 ($X^1\Sigma_g^+$). The dotted line represents the total loss rate of N_2 ($B^3\Pi_g$).

G7 and G8) but with much lower rate values. Processes G1, G2 and G3 exhibit a very sharp decrease at the end of the pulse when intersystem collisional transfer reactions, the processes G7 and G8, reach their maximum values. Processes G7 and G8 prevail over G1 up to three milliseconds. According to the present sprite kinetic model, energy pooling reactions (as suggested by *Kamaratos* [2009]) are negligible for producing N_2 ($B^3\Pi_g$, v = 0–6). According to Figure 9b, the main loss channels of N_2 ($B^3\Pi_g$, v = 2) are radiative de-excitation to N_2 ($A^3\Sigma_u^+$, v = 1) and N_2 ($A^3\Sigma_u^+$, v = 0), that is, processes L1 and L2, respectively. The loss of N_2 ($B^3\Pi_g$, v = 2) concentration due to collisional channels, mainly ICT (L5), play a marginal role.

[41] The vibrational distribution function of N_2 ($B^3\Pi_g$) (populations of vibrational levels within the electron state $B^3\Pi_g$ relative to v = 2) for different times from 0.1 μs to 10 ms is shown in Figure 10. None of the VDFs shown in Figure 10 peak at v = 2 and their shape indicate certain deviation (more pronounced for longer times) from an equilibrium VDF of N_2 ($B^3\Pi_g$) over the vibrationally excited states considered from v = 0 to v = 6.

[42] Figure 11a shows the experimental vibrational distribution function of N_2 ($B^3\Pi_g$) at different altitudes for vibrational levels from v = 2 to v = 7 as obtained by *Kanmae et al.* [2007] using high-speed video recording (300 fps or 3 ms time resolution) from sprite spectra in the 640 nm–820 nm and with spectral resolution of 3 nm. In addition, Figure 11a includes dashed (52.7–55 km), dotted (72.7–75 km) and dashed-dotted (84.4–86.4 km) lines that represent fits of the experimental VDFs to equilibrium Boltzmann vibrational distributions carried out in the present work. The Boltzmann VDFs fit quite well the available experimental VDF of N_2 ($B^3\Pi_g$) when the ground and first vibrational levels of N_2 ($B^3\Pi_g$) are disregarded (the spectral region experimentally covered only reaches up to 820 nm [*Kanmae et al.*, 2007]). Considering uncertainties of ±10%, T^B_{vib} ~ 5500 K is the best fit vibrational temperature for the three fits shown in Figure 11a. Thus, it appears from Figure 11a that the vibrational distribution of N_2 ($B^3\Pi_g$) is in equilibrium. The latter is confirmed when looking at Figure 11b, where the calculated VDF for N_2 ($B^3\Pi_g$) (with v = 0 through 6) at 78 km and averaged over 3 ms (300 fps speed recording) is represented together with the VDF for N_2 ($B^3\Pi_g$) (with v = 2 through 7) as recorded by *Kanmae et al.* [2007] at 300 fps for 72.7–75 km. The dashed and dashed-dotted straight lines in Figure 11b are Boltzmann VDF fits to the calculated and experimental VDFs of N_2 ($B^3\Pi_g$), respectively.

[43] To conclude, Figure 12 shows the calculated vibrational distribution function of N_2 ($B^3\Pi_g$) at 78 km averaged over 30 ms or 30 fps; 3 ms or 300 fps and 0.1 ms or 10000 fps and the experimental VDF as derived by *Kanmae et al.* [2007] for N_2 ($B^3\Pi_g$) using high-speed video recording (3 ms time resolution or 300 fps) from sprite spectra recorded in the 640 nm–820 nm range with spectral resolution of 3 nm and for altitudes between 72.7 and 75 km. There is a very good agreement between the recently measured N_2 ($B^3\Pi_g$) VDF at 300 fps [*Kanmae et al.*, 2007] and the predicted VDF by the present model for approximately the same altitude and considering the vibrational levels from v = 2 to v = 6 (the ones covered by available observations). The predicted N_2 ($B^3\Pi_g$) VDF shown in Figure 12 goes beyond v = 2 and indicates that

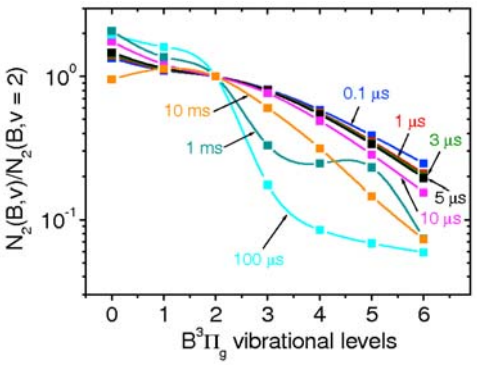

Figure 10. Calculated vibrational distribution function (VDF) of N_2 ($B^3\Pi_g$) for different times from 0.1 μs to 10 ms.

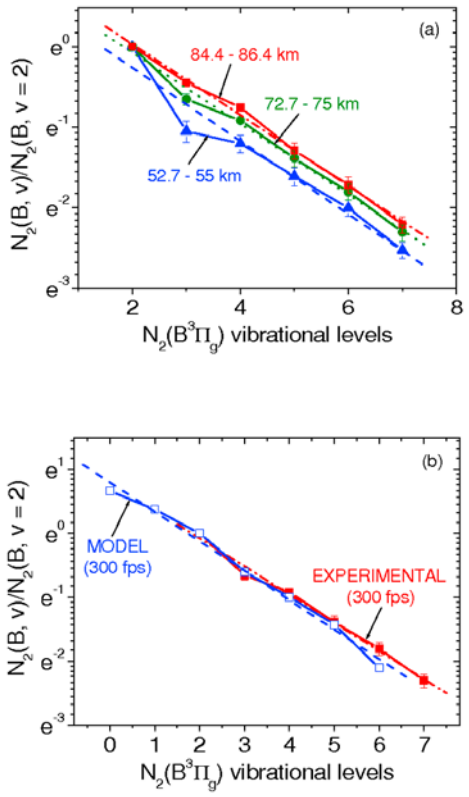

Figure 11. (a) Experimental vibrational distribution function (VDF) of N_2 ($B^3\Pi_g$) at different altitudes for vibrational levels from v = 2 to v = 7 as obtained by *Kanmae et al.* [2007] using high-speed video recording (300 fps or 3 ms time resolution) from sprite spectra in the 640–820 nm range with spectral resolution of 3 nm. The dashed (52.7–55 km), dotted (72.7–75 km), and dashed-dotted (84.4–86.4 km) lines represent fits of the experimental VDFs to Boltzmann VDF carried out in the present work; considering the errors in the experimental VDF shown, the associated vibrational temperature of the N_2 ($B^3\Pi_g$) state derived from the Boltzmann fits is 5500 K. (b) Comparison between the experimental (solid squares) VDF of N_2 ($B^3\Pi_g$) recorded at 300 fps for the altitude range 72.7–75 km and the calculated (open squares) VDF of N_2 ($B^3\Pi_g$) averaged over 3 ms (300 fps speed recording) as obtained from the present model at 78 km. The dashed and dashed-dotted lines correspond to the Boltzmann fits of the calculated and experimental VDFs, respectively.

there is no enhancement at v = 2. The second positive group of N_2, that is, radiative emissions from N_2 ($C^3\Pi_u$, v) toward N_2 ($B^3\Pi_g$, v = 2) is the key mechanism that prevents the enhancement of the N_2 ($B^3\Pi_g$) VDF at v = 2. When emissions from N_2 ($C^3\Pi_u$, v) are removed from the model, the concentration of N_2 ($B^3\Pi_g$, v = 2) dominates over the ones of v = 0 and v = 1 causing an enhancement of the N_2 ($B^3\Pi_g$) VDF at v = 2.

[44] The emissions from N_2 ($B^3\Pi_g$, v = 0, 1) have not yet been studied by spectroscopic means at this altitude (72–78 km) although a paper by *Morrill et al.* [1998] (and later on *Bucsela et al.* [2003]) observationally showed that the vibrational populations of the N_2 ($B^3\Pi_g$) associated to sprite spectra at 57 km peaks at v = 2 (although this result might be probably due to sensitivity calibration errors as mentioned by *Bucsela et al.* [2003]); however, the same vibrational populations of N_2 ($B^3\Pi_g$) recorded at 53 km by *Bucsela et al.* [2003] did not exhibit any enhancement at v = 2. Therefore, it is clear that new measurements are needed.

[45] The present sprite kinetic model also predicts that if the N_2 ($B^3\Pi_g$) VDF were recorded by using very high speed video cameras at 10000 fps, the resulting VDF would only take slightly higher values (in the v = 2 through v = 6 region) than the measured N_2 ($B^3\Pi_g$) VDF as observed at 300 fps or even at 30 fps.

[46] Finally, the shape of the calculated N_2 ($B^3\Pi_g$) VDF as shown in Figure 12 is close to a Boltzmann (equilibrium) vibrational distribution equilibrium even when v = 0 and v = 1 are considered.

3.6. Vibrational Kinetics of N_2 ($C^3\Pi_u$)

[47] The present model has also allowed us to study the vibrational kinetics of the five (v = 0–4) lower vibrational levels of N_2 ($C^3\Pi_u$). The main production channel of vibrationally excited N_2 ($C^3\Pi_u$) is direct electron-impact excitation from N_2 ($X^1\Sigma_g^+$), that is, N_2 ($X^1\Sigma_g^+$, v = 0) + e → N_2 ($C^3\Pi_u$, v = 0–4) + e. However, at 5 μs, the population of N_2 ($C^3\Pi_g$, v = 0–3) becomes controlled by process N_2 ($C^3\Pi_u$, v ≥ 1) + N_2 ($X^1\Sigma_g^+$, v = 0) → N_2 ($C^3\Pi_g$, v−1) + N_2 ($X^1\Sigma_g^+$, v = 1). The loss of vibrationally excited N_2 ($C^3\Pi_u$) is mainly due to cascade radiative de-excitation toward different vibrational levels of N_2 ($B^3\Pi_g$).

[48] The VDF of N_2 ($C^3\Pi_u$) for different times from 0.1 μs to 10 ms is shown in Figure 13a. In addition, Boltzmann VDFs (straight dashed lines) have been fitted to the calculated VDFs. The agreement between the Boltzmann and the calculated VDFs is quite reasonable. The latter indicates that the VDF of N_2 ($C^3\Pi_u$) is in equilibrium and that a vibrational temperature (T^C_{vib}) can be associated to N_2 ($C^3\Pi_u$) for the different times investigated. It is found that T^C_{vib} takes the values ~10500 K (0.1 μs), ~3200 K (3 μs), ~2900 K (5 μs) and ~1660 K (100 μs, 10 ms and 100 ms).

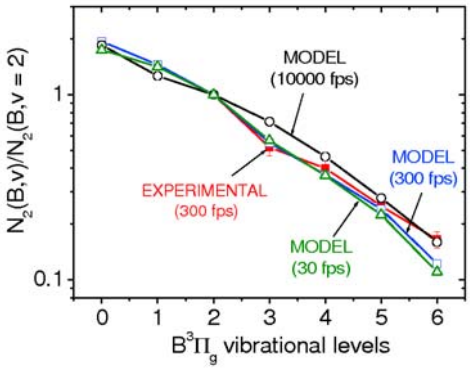

Figure 12. Calculated vibrational distribution function (VDF) of N_2 ($B^3\Pi_g$) at 78 km averaged over 30 ms or 30 fps (open triangles); 3 ms or 300 fps (open squares); and 0.1 ms or 10000 fps (open circles) and the experimental VDF (solid squares) as derived by *Kanmae et al.* [2007] for N_2 ($B^3\Pi_g$) using high-speed video recording (3 ms time resolution or 300 fps) from sprite spectra recorded in the 640–820 nm range with spectral resolution of 3 nm and for altitudes between 72.7 and 75 km.

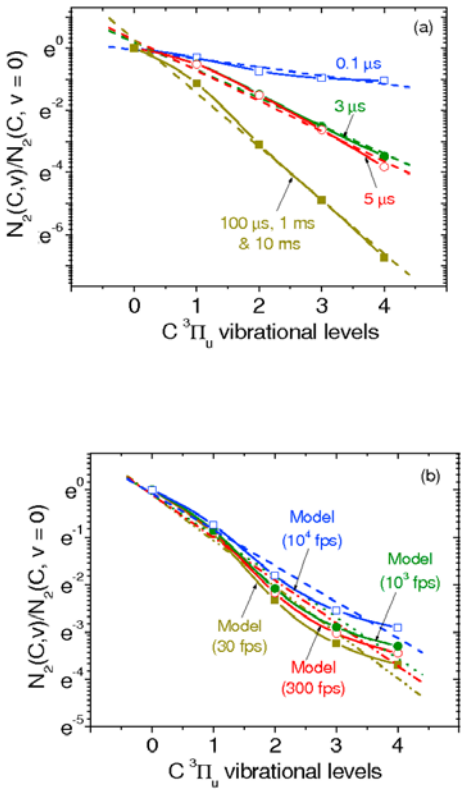

Figure 13. (a) Calculated vibrational distribution function (VDF) of N_2 ($C^3\Pi_u$) for different times (0.1 μs, open squares; 3 μs, solid circles; 5 μs, open circles; 100 μs, 10 ms, and 100 ms, solid squares) and corresponding fits to Boltzmann VDFs (dashed lines) which provides reasonable estimates for $C^3\Pi_u$ vibrational temperatures of 10500 K (0.1 μs), 3200 K (3 μs), 2900 K (5 μs), and 1660 K (100 μs, 10 ms, and 100 ms). (b) Calculated VDF of N_2 ($C^3\Pi_u$) averaged over 30 ms (solid squares), 3 ms (open circles), 1 ms (solid circles), and 0.1 ms (open squares) and their corresponding Boltzmann VDF fits (30 ms, dashed-dotted-dotted line; 3 ms, dashed-dotted line; 1 ms, dotted line; 0.1 ms, dashed line).

[49] The calculated VDF of N_2 ($C^3\Pi_u$) averaged over periods of times of 30 ms, 3 ms and 1 ms has been represented in Figure 13b together with Boltzmann (equilibrium) VDFs represented by straight lines. As can be seen in Figure 13b, the calculated sprite induced VDFs of N_2 ($C^3\Pi_u$) at 78 km are close to equilibrium values. The VDFs of N_2 ($C^3\Pi_u$) shown in Figure 13b are predictions about how field recorded VDFs of N_2 ($C^3\Pi_u$) would look like when using video cameras working at different speeds (30 fps, 300 fps, 1000 fps and 10000 fps) coupled to imaging spectrographs tuned in the appropriate spectral range.

4. Conclusions

[50] This paper has been devoted to study the vibrational kinetics of sprite plasmas with special attention in the analysis of the vibrational kinetics of N_2 ($B^3\Pi_g$) and N_2 ($C^3\Pi_u$) involved in the characteristic red and blue emissions from sprites. It has been found that the integrated (averaged over different time periods) vibrational distribution functions of N_2 ($X^1\Sigma_g^+$) and N_2 ($A^3\Sigma_u^+$) are far from equilibrium (Boltzmann) values while the averaged VDFs of N_2 ($B^3\Pi_g$) and N_2 ($C^3\Pi_u$) are close to equilibrium distributions. However, we also found that the time-dependent VDF of N_2 ($A^3\Sigma_u^+$) and N_2 ($C^3\Pi_u$) are close to equilibrium and that, consequently, the vibrational temperatures of the $A^3\Sigma_u^+$ and $C^3\Pi_u$ states of N_2 decreases from ~10000 K to ~3700 K (case of $A^3\Sigma_u^+$) and to ~1600 K (case of $C^3\Pi_u$) as time increases from 1 μs to 10 ms.

[51] In connection with the mechanisms controlling the production of N_2 ($B^3\Pi_g$, v = 2), we found that, during the pulse (times $\lesssim$ 5 μs), energy pooling is negligible for producing N_2 ($B^3\Pi_g$, v = 2) while direct electron-impact excitation from N_2 ($X^1\Sigma_g^+$) dominates but closely followed by radiative cascade de-excitation from N_2 ($C^3\Pi_u$, v = 0–4). After the pulse, intersystem collisional transfer is the most important production channel of N_2 ($B^3\Pi_g$, v = 2) up to about several milliseconds, then direct electron-impact excitation from N_2 ($X^1\Sigma_g^+$) becomes dominant. The removal of N_2 ($B^3\Pi_g$, v = 0–6) at anytime is mainly due to radiative decays toward different vibrational levels of N_2 ($A^3\Sigma_u^+$) state.

[52] The calculated vibrational distribution function of N_2 ($B^3\Pi_g$) exhibits a good agreement with available observationally measured VDF of N_2 ($B^3\Pi_g$) at 300 fps ($\Delta t = 3$ ms) and altitudes 73–78 km. The model-predicted VDF of N_2 ($B^3\Pi_g$) shows no enhancement at v = 2. Such enhancement would appear if radiative cascade from N_2 ($C^3\Pi_u$) to N_2 ($B^3\Pi_g$) were not considered. In addition, the present sprite kinetic model predicts that the expected VDFs of N_2 ($B^3\Pi_g$) and N_2 ($C^3\Pi_u$) recorded at 10000 fps would not differ much from the ones obtained at lower time resolutions of 3 ms (300 fps) or even 30 ms (30 fps).

[53] Finally, we think that, in the near future, it would be important to carry out more spectroscopic observations in the blue-green (300–550 nm) and near infrared (900–1.4 μm) spectral regions. This would give access to vibrational information of the N_2 ($C^3\Pi_u$) state and, on the other hand, will also provide spectral observations that could reveal information on the populations of the lower vibrational levels (v = 0 and v = 1) of N_2 ($B^3\Pi_g$). The above mentioned spectroscopic studies on emissions from N_2 ($C^3\Pi_u$) and N_2 ($B^3\Pi_g$) will allow comparison of observational results with present and future model predictions.

Appendix A

[54] Ground neutrals considered: N, N_2, O, O_2, O_3, NO, NO_2, NO_3, N_2O, CO, CO_2, Ar.

[55] Electronically excited neutrals: N_2 ($A^3\Sigma_u^+$, $B^3\Pi_g$, $W^3\Delta_u$, $B'^3\Sigma_u^-$, $C^3\Pi_u$) N_2 ($a'^1\Sigma_u^-$, $a^1\Pi_g$); O_2 ($a^1\Delta_g$, $b^1\Sigma_g^+$), O (^{1}D, ^{1}S); NO ($A^2\Sigma^+$), N (^{2}D, ^{2}P).

[56] Vibrationally excited neutrals considered: N_2 ($X^1\Sigma_g^+$ (v = 0–8)); N_2 ($A^3\Sigma_u^+$ (v = 0–16)); N_2 ($B^3\Pi_g$ (v = 0–6)); N_2 ($C^3\Pi_u$ (v = 0–4)); N_2 ($W^3\Delta_u$ (v = 0–3)); N_2 ($B'^3\Sigma_u^-$ (v = 0, 1)); CO_2 (001, 010, 100).

[57] Electrons and negative ions considered: e, O^-, O_2^-, O_3^-, NO^-, NO_2^-, NO_3^-, CO_3^-, CO_4^-.

[58] Positive ions considered: N_2^+, N_4^+, O^+, O_2^+, NO^+, NO_2^+, N_2O^+, $N_2O_2^+$, Ar^+.

[59] **Acknowledgments.** The author acknowledges partial financial support provided by MICINN under Projects AYA2009-14027-C05-02, MAT2006-13006-C02-01, and ENE2006-14577-C04-03. The author also wishes to thank the conveners (Davis D. Sentman, Victor P. Pasko, and Jeff S. Morrill) of the AGU Chapman Conference on Effects of Thunderstorms and Lightning in the Upper Atmosphere for organizing a stimulating conference on the campus of Pennsylvania State University at State College in May 2009. Finally, the author would also like to thank Vasco Guerra for some comments on the possible importance of some V-T reactions.

[60] Amitava Bhattacharjee thanks George Naidis and Jeff Morrill for their assistance in evaluating this paper.

References

Adachi, T., et al. (2008), Electric and electron energies in sprites and temporal evolutions of lightning charge moment, *J. Phys. D Appl. Phys.*, *41*, 234010, doi:10.1088/0022-3727/41/23/234010.

Billing, G. D., and E. R. Fisher (1979), VV and VT rate coefficients in N_2 by a quantum-classical model, *Chem. Phys.*, *43*, 395–401, doi:10.1016/0301-0104(79)85207-6.

Borst, W. L., and S. L. Chang (1973), Excitation of metastable N_2 ($A^3\Sigma_u^+$) vibrational levels by electron impact, *J. Chem. Phys.*, *59*, 5830–5836, doi:10.1063/1.1679950.

Bourdon, A., V. P. Pasko, N. Y. Liu, S. Célestin, P. Ségur, and E. Marode (2007), Efficient models for photoionization produced by non-thermal gas discharges in air based on radiative transfer and the Helmholtz equations, *Plasma Sources Sci. Technol.*, *16*, 656–678, doi:10.1088/0963-0252/16/3/026.

Bucsela, E., J. Morrill, M. Heavner, C. Siefring, S. Berg, D. Hampton, D. Moudry, E. Wescott, and D. Sentman (2003), N_2 ($B^3\Pi_g$) and N_2^+ ($A^2\Pi_u$) vibrational distributions observed in sprites, *J. Atmos. Sol. Terr. Phys.*, *65*, 583–590, doi:10.1016/S1364-6826(02)00316-4.

Caledonia, G. E., and R. E. Center (1971), Vibrational distribution functions in anharmonic oscillators, *J. Chem. Phys.*, *55*, 552–561, doi:10.1063/1.1675787.

Calo, J. M., and R. C. Axtmann (1971), Vibrational relaxation and electronic quenching of N_2 ($C^3\Pi_u$, v = 1) of nitrogen, *J. Chem. Phys.*, *54*, 1332–1341, doi:10.1063/1.1674973.

Capitelli, M., C. M. Ferreira, B. F. Gordiets, and A. I. Osipov (2000), *Plasma Kinetics in Atmospheric Gases*, Springer, Berlin.

Cartwright, D. C. (1978), Vibrational populations of the excited state of N_2 under auroral conditions, *J. Geophys. Res.*, *83*, 517–531, doi:10.1029/JA083iA02p00517.

Cartwright, D. C., S. Trajmar, A. Chutjian, and W. Williams (1977), Electron impact excitation of the electronic states of N_2. II. Integral cross sections at incident energies from 10 to 50 eV, *Phys. Rev. A*, *16*, 1041–1051, doi:10.1103/PhysRevA.16.1041.

Collins, W. D., et al. (2004), Description of the NCAR Community Atmospheric Model (CAM3), *Tech. Rep. NCAR/TN-464 STR*, Natl. Cent. for Atmos. Res, Boulder, Colo.

Gear, C. W. (1971), *Numerical Initial Value Problems in Ordinary Differential Equations*, Prentice-Hall, New York.

Gilmore, F. R., R. R. Laher, and P. J. Espy (1992), Franck-Condon factors, r-centroids, electronic transition moments, and Einstein coefficients for many nitrogen and oxygen band systems, *J. Phys. Chem. Ref. Data*, *21*, 1005–1107.

Gordiets, B., and A. Ricard (1993), Production of N, O and NO in N_2-O_2 flowing discharges, *Plasma Sources Sci. Technol.*, *2*, 158–163, doi:10.1088/0963-0252/2/3/005.

Gordiets, B., C. M. Ferreira, V. Guerra, J. Loureiro, J. Nahorny, D. Pagnon, M. Touzeau, and M. Vialle (1995), Kinetic model of a low-pressure N_2-O_2 flowing glow discharge, *IEEE Trans. Plasma Sci.*, *23*, 750–768, doi:10.1109/27.467998.

Gordillo-Vazquez, F. J. (2008), Air plasma kinetics under the influence of sprites, *J. Phys. D Appl. Phys.*, *41*, 234016, doi:10.1088/0022-3727/41/23/234016.

Green, B. D., M. E. Fraser, W. T. Rawlins, L. Jeong, W. A. M. Blumberg, S. B. Mende, G. R. Swenson, D. L. Hampton, E. M. Wescott, and D. D. Sentman (1996), Molecular excitation in sprites, *Geophys. Res. Lett.*, *23*, 2161–2164, doi:10.1029/96GL02071.

Guerra, V. (1998), Estudio cinético de descargas luminescentes em gases moleculares: Applicação à mistura N_2-O_2, PhD. thesis, Univ. Técnica de Lisboa, Lisbon.

Hampton, D. L., M. J. Heavner, E. M. Wescott, and D. D. Sentman (1996), Optical spectral characteristics of sprites, *Geophys. Res. Lett.*, *23*, 89–92, doi:10.1029/95GL03587.

Heavner, M., D. Sentman, D. Moudry, E. Wescott, C. Siefring, J. Morrill, and E. Bucsela (2000), Blue jets and elves: Optical evidence of energy transport across the stratopause, in *Atmospheric Science Across the Stratopause*, *Geophys. Monogr. Ser.*, vol. 123, edited by D. E. Siskind, S. D. Eckerman, and M. E. Summers, pp. 69–82, AGU, Washington, D. C.

Kamaratos, E. (2009), Comment on "Plasma chemistry of sprite streamers" by D. D. Sentman, H. C. Stenbaek-Nielsen, M. G. McHarg, and J. S. Morrill, *J. Geophys. Res.*, *114*, D08109, doi:10.1029/2008JD011196.

Kanmae, T., H. C. Stenbaek-Nielsen, and M. G. McHarg (2007), Altitude resolved sprite spectra with 3 ms temporal resolution, *Geophys. Res. Lett.*, *34*, L07810, doi:10.1029/2006GL028608.

Kuo, C. L., R. R. Hsu, A. B. Chen, H. T. Su, L. C. Lee, S. B. Mende, H. U. Frey, H. Fukunishi, and Y. Takahashi (2005), Electric fields and electron energies inferred from the ISUAL recorded sprites, *Geophys. Res. Lett.*, *32*, L19103, doi:10.1029/2005GL023389.

Kurnosov, A., A. Napartovich, S. Shnyrev, and M. Cacciatore (2007), Vibrational energy exchanges in nitrogen: Application of new rate constants for kinetic modeling, *J. Phys. Chem. A*, *111*, 7057–7065, doi:10.1021/jp071657a.

Liu, N., and V. P. Pasko (2004), Effects of photoionization on propagation and branching of positive and negative streamers in sprites, *J. Geophys. Res.*, *109*, A04301, doi:10.1029/2003JA010064.

Liu, N., et al. (2006), Comparison of results from sprite streamer modeling with spectrophotometric measurements by ISUAL instrument on FORMOSAT-2 satellite, *Geophys. Res. Lett.*, *33*, L01101, doi:10.1029/2005GL024243.

McHarg, M. G., H. C. Stenbaek-Nielsen, and T. Kammae (2007), Observations of streamer formation in sprites, *Geophys. Res. Lett.*, *34*, L06804, doi:10.1029/2006GL027854.

Mende, S. B., R. L. Rairden, G. R. Swenson, and W. A. Lyons (1995), Sprite spectra; N_2 1 PG band identification, *Geophys. Res. Lett.*, *22*, 2633–2636, doi:10.1029/95GL02827.

Mishin, E. V., and G. M. Milikh (2008), Blue jets: Upward lightning, *Space Sci. Rev.*, *137*, 473–488, doi:10.1007/s11214-008-9346-z.

Moore, C. B., R. E. Wood, B. L. Hu, and J. T. Yardley (1967), Vibrational energy transfer in CO_2 lasers, *J. Chem. Phys.*, *46*, 4222–4231, doi:10.1063/1.1840527.

Morrill, J. S., and W. M. Benesch (1996), Auroral N_2 emissions and the effect of collisional processes on N_2 triplet state vibrational populations, *J. Geophys. Res.*, *101*, 261–274, doi:10.1029/95JA02835.

Morrill, J. S., E. J. Bucsela, V. P. Pasko, S. L. Berg, M. J. Heavner, D. R. Moudry, W. M. Benesch, E. M. Wescott, and D. D. Sentman (1998), Time resolved N_2 triplet state vibrational populations and emissions associated with red sprites, *J. Atmos. Sol. Terr. Phys.*, *60*, 811–829, doi:10.1016/S1364-6826(98)00031-5.

Morrill, J. S., et al. (2002), Electron energy and electric field estimates in sprites derived from ionized and neutral N_2 emissions, *Geophys. Res. Lett.*, *29*(10), 1462, doi:10.1029/2001GL014018.

Pintassilgo, C. D., O. Guaitella, and A. Rousseau (2009), Heavy species kinetics in low-pressure dc pulsed discharge in air, *Plasma Sources Sci. Technol.*, *18*, doi:10.1088/0963-0252/18/2/025005.

Piper, L. G. (1988a), State-to-state N_2 ($A^3\Sigma_u^+$) energy pooling reactions. II. The formation and quenching of N_2 ($B^3\Pi_g$, v′ = 1–12), *J. Chem. Phys.*, *88*(11), 6911–6921, doi:10.1063/1.454388.

Piper, L. G. (1988b), State-to-state N_2 ($A^3\Sigma_u^+$) energy pooling reactions. I. The formation of N_2 ($C^3\Pi_u$), *J. Chem. Phys.*, *88*(1), 231–239, doi:10.1063/1.454649.

Piper, L. G. (1989), The excitation of N_2 ($B^3\Pi_g$, v = 1–12) in the reaction between N_2 ($A^3\Sigma_u^+$) and N_2(X, v ≥ 5), *J. Chem. Phys.*, *91*(2), 864–873, doi:10.1063/1.457138.

Sentman, D. D., H. C. Stenbaek-Nielsen, M. G. McHarg, and J. S. Morrill (2008), Plasma chemistry of sprite streamers, *J. Geophys. Res.*, *113*, D11112, doi:10.1029/2007JD008941. (Correction, *J. Geophys. Res.*, *113*, D14399, doi:10.1029/2008JD010634, 2008.)

Simek, M. (2002), The modelling of streamer-induced emission in atmospheric pressure, pulsed positive corona discharge: N_2 second positive and NO-γ systems, *J. Phys. D Appl. Phys.*, *35*, 1967–1980, doi:10.1088/0022-3727/35/16/311.

Stenbaek-Nielsen, H. C., and M. G. McHarg (2008), High-time resolution sprite imaging: Observations and implications, *J. Phys. D Appl. Phys.*, *41*, 234009, doi:10.1088/0022-3727/41/23/234009.

Stenbaek-Nielsen, H. C., M. G. McHarg, T. Kanmae, and D. D. Sentman (2007), Observed emission rates in sprite streamer heads, *Geophys. Res. Lett.*, *34*, L11105, doi:10.1029/2007GL029881.

F. J. Gordillo-Vazquez, Instituto de Astrofísica de Andalucía, CSIC, P.O. Box 3004, E-18080 Granada, Spain. (vazquez@iaa.es)